Computational Geosciences (2022) 26:1011–1028
https://doi.org/10.1007/s10596-021-10109-3

ORIGINAL PAPER

Multiscale matrix-fracture transfer functions for naturally fractured reservoirs using an analytical, infinite conductivity, discrete fracture model

R. D. Hazlett[1] · R. Younis[2]

Received: 7 January 2021 / Accepted: 27 September 2021 / Published online: 22 October 2021

Abstract
Fracture matrix transfer functions have long been recognized as tools in modelling naturally fractured reservoirs. If a significant degree of fracturing is present, models involving single matrix blocks and matrix block distributions become relevant. However, this captures only the largest fracture sets and treats the matrix blocks as homogeneous, though possibly anisotropic. Herein, we produce the steady and transient baseline solutions for depletion for such models. Multiscale models pass below grid scale information to the larger scale system with some numerical cost. Instead, for below block scale information, we take the analytic solution to the Diffusivity Equation for transient inflow performance of wells of arbitrary trajectory, originally developed for Neumann boundary conditions, and recast it for Dirichlet boundaries with possible internal fractures of variable density, length, and orientation. As such, it represents the analytical solution for a heterogeneous matrix block surrounded by a constant pressure sink, we take to be the primary fracture system. Instead of using a constant rate internal boundary condition on a fracture surrounded by matrix, we segment the fracture and, through imposed material balance, force the internal complex fracture feature to be a constant pressure element with net zero flux. In doing so, we create a representative matrix block with infinite conductivity subscale fractures that impact the overall drainage into the surrounding fracture system. We vary the internal fracture structure and delineate sensitivity to fracture spacing and extent of fracturing. We generate the complete transient solution, enabling new well test interpretation for such systems in characterization of block size distributions or extent of below block-scale fracturing. The initial model for fully-penetrating fractures can be extended to 3D, generalized floating fractures of arbitrary inclination, and internal complex fracture networks.

Keywords Fracture · Transfer · Multiscale · Analytical · Diffusivity · Transients

1 Background

Modelling of naturally fractured reservoirs has proven necessary but difficult. The abundance of hydrocarbon resources associated with naturally fractured reservoirs justifies the need. Difficulties are born out of the disparity between the scale of the prevailing physics and the physical size of the solution domain. Furthermore, we have interacting systems with large contrast in porosity and permeability. Thus, we have discretization and numerical stability issues, making such simulations notoriously challenging. Recovery from such systems is also low due to the inability to control matrix displacement. Wells communicate with the dominant hydrocarbon storage medium predominantly through fracture face boundary conditions, and often the underlying physics at such boundaries controls the extraction process.

The demand to handle high permeability, low capacity fractures alongside low permeability, high capacity matrix naturally led researchers to decompose the reservoir into an interacting systems model. We define two systems and an interaction through an exchange function – the matrix-fracture transfer function. The fidelity of the model is dependent upon the relevance of the reservoir description and the adequacy of the matrix-fracture transfer function to portray the

✉ R. D. Hazlett
randy.hazlett@nu.edu.kz

[1] School of Mining and Geosciences, Nazarbayev University, Kabanbay Batyr Ave 53, Nur-Sultan, Kazakhstan 010000

[2] McDougall School of Petroleum Engineering, The University of Tulsa, 800 S Tucker Dr, Tulsa, OK 74104, USA

physics of pore-scale phenomena along with the necessary scale-up processes. Early models simplified the reservoir system to a representative matrix block surrounded by fractures. These models were generalized and improved and, surprisingly, still are considered a mainstay in the characterization of production from naturally fractured reservoirs [1].

There has been much progress on the numerical solution of systems with multiscale phenomena in space and time that lend to the improved simulation of naturally fractured reservoirs. Researchers have experimented with different approaches to capture the effects of contributing physics at different scales. Among these include Embedded Discrete Fracture Models (EDFM) and Multiple INteracting Continua (MINC) or nested layers in gridding [2]. Bosma et al. [3] presented a multiscale method for discrete fracture modelling using unstructured grids where grids at one scale feed information to another that conforms to fracture geometry. Xu and Sepehrnoori [4] developed an embedded discrete fracture model that takes advantage of corner point grids with the advantage of compatibility with commercial simulators.

Others have sought transfer functions to capture the interaction between the matrix blocks and fractures [5–9], namely, how the average pressure and/or saturation within a grid block should behave in time after a disturbance at the boundary without having to spatially resolve it. Since numerical simulators only deal with block average properties, such transfer functions look attractive, if they can reliably depict the subscale physics. In this manner, blocks deplete and expel into the fracture system, and tracking averages allows for conservation of mass. This effectively means that someone has solved the problem already on a fine grid and stored the solution somewhere [8, 10]. If a large enough database of reliable functions exists, it might solve most problems in modelling naturally fractured reservoirs.

Maier and Geiger [11] demonstrated multi-rate dual porosity models that introduce a distribution of transfer functions per block to capture more variability in properties, including the effects of smaller-scale fractures, in conjunction with a discrete fracture model that captures the largest fracture sets. Belani and Jalali [12] examined pseudo-steady state and transient model behaviour for uniform and bimodal block size distributions but employed solutions with radial symmetry and an infinite acting boundary condition. Interestingly, these authors noted that a closed form analytical solution was unavailable to describe transient flow. Contrary to the paper title, theirs is a forward model for prescribed block size distribution. Gong and Rossen [13] tried to reduce dual permeability fractured reservoir simulation to the determination of shape factors (transfer functions) on only the dominant fluid-carrying fracture subset. Amiry [14] gave an insightful summary of state-of-the-art naturally fractured reservoir modelling and carefully proposed a method within computational reach for real world applications that captured subscale information in matrix blocks. He proposed scaled matrix recovery curves to prescribe transfer functions coming from experiments or single block simulations. Whereas, Bosma et al. [3] developed a multiscale, embedded discrete fracture, finite volume method, underpinned by fine grid numerical simulation, to capture the effect of below grid fracture flow behaviour. All these methods are valid means to interject more meaningful physics from the scale at which displacement occurs onto a more computationally tractable, coarse scale numerical scheme.

2 Theory

We propose a hybrid model that relies on Green's function solutions representing anisotropic matrix blocks of variable size that are surrounded by fractures but also contain underlying internal discrete complex fractures. Hazlett and Babu [15, 16] developed an analytic, arbitrary orientation, discrete line source well model that was shown to also be capable of modelling complex fractures in two dimensions. That model was developed for Neumann boundary conditions. In another publication, Hazlett [17] demonstrated how the Neumann boundary condition solution can be generalized to open systems using boundary integral methods. In particular, the uniform flux boundary condition was shown to be readily modelled analytically. Here, the Dirichlet boundary condition is most appropriate. Thus, following the methodology of Hazlett and Babu [15], we construct the analogous analytic solution for uniform pressure boundaries of a matrix block in two dimensions containing an arbitrarily-oriented line source, representing a discrete fracture. Using superposition, this can be generalized to complex fracture systems within the matrix block surrounded by the primary fracture network. These fractures, however, do not serve as sources, but only conduits to short circuit some fraction of flow in porous media. Consequently, we segment the fractures and enforce a net zero flux condition. Material entering a fracture can exit elsewhere; thus, these internal fractures alter the macroscopic properties of the matrix block as sort of superhighways for fluid migration. The zero-flux constraint is essentially a material balance on the composite fracture. Thus, the fractures will appear in the solution as infinite conductivity streaks. The goal is then to be able to quantify the impact of these features that are below the resolution of the matrix block on the properties of the block, and, in particular, how this influences the physics at the fracture-matrix boundary of the primary fracture network. In such a modelling approach, we assume recovery of material entering the primary fracture system is not the rate limiting step. All steps performed for a 2D system are amenable to 3D generalization.

2.1 Anisotropic, homogeneous matrix block behaviour with a source

We start with a development for the pressure transient behaviour of an anisotropic matrix block. While some have used pseudo-steady state fracture-matrix transfer functions, the interest in pressure transient interpretation for improved characterization of naturally fractured reservoirs prompts us to start with transient solutions. The time period for transients to die out is likewise of interest. Also, while there may be interest in the pressure distribution, we want to capture the boundary flux distribution and the average pressure change with time. The benefit of an analytical solution is that we have a solution for arbitrary observation point that can support a wide variety of queries.

Limiting our investigation to single phase solutions for pressure, we seek the solution to the 1-D Heat Equation with internal source

$$\kappa \frac{\partial^2 u}{\partial x^2} + f = \frac{\partial u}{\partial t} \tag{1}$$

where κ is the diffusivity, f is a source function, and we will interpret u as pressure. Carslaw and Yeager [18] gave us one solution on a domain of length, a, with zero flux at the boundaries and source at x_o as

$$u = 1 + 2\sum_{l=1}^{\infty} e^{-(\pi l)^2 \left(\frac{k}{a^2}\right) t_D} \cos\left(\frac{\pi l x}{a}\right) \cos\left(\frac{\pi l x_o}{a}\right) \tag{2}$$

where we have introduced a dimensionless time, t_D, and a characteristic length as the square root of the permeability, $\sqrt{k}$.

This solution is immediately expanded through the Neuman Product Rule [19] to higher dimensional solutions. In the present application, we stop with 2D with the expectation of vertical, fully-penetrating fractures. This could later be relaxed, as needed. This particular form of the solution marches backwards in time from the pseudo-steady state (PSS) result. We note that singularities are in space and not time, so the PSS result contains all the necessary singularity handling. The solution is easy to prescribe, but computational challenging [15]. We make use of the constant rate point source solution subject to a uniform pressure initial condition and either Neumann or Dirichlet boundaries.

2.1.1 Pseudo-Steady State Behaviour

While we have the Neumann Function (sealed boundary) pseudo-steady state solution for a 2D box of dimension a x b with directional permeabilities, k_x, and k_y as

$$N(x,y;x_o,y_o) = \frac{2^{\mathrm{d}}}{\pi^2 ab} \sum_{l,m\neq 0} \frac{\cos\left(\frac{\pi l x}{a}\right)\cos\left(\frac{\pi m y}{b}\right)\cos\left(\frac{\pi l x_o}{a}\right)\cos\left(\frac{\pi m y_o}{b}\right)}{k_x \frac{l^2}{a^2} + k_y \frac{m^2}{b^2}} \tag{3}$$

where N represents the pressure difference between the pressure at (x, y) and the average pressure, $\overline{p}$, with a unit point source at (x_o,y_o), the analogous pressure distribution for Dirichlet boundary conditions [20] is given as

$$G(x,y;x_o,y_o) = \frac{2^{\mathrm{d}}}{\pi^2 ab} \sum_{l,m\neq 0} \frac{\sin\left(\frac{\pi l x}{a}\right)\sin\left(\frac{\pi m y}{b}\right)\sin\left(\frac{\pi l x_o}{a}\right)\sin\left(\frac{\pi m y_o}{b}\right)}{k_x \frac{l^2}{a^2} + k_y \frac{m^2}{b^2}} \tag{4}$$

Note we simply switch cosines to sines in the solution to satisfy external boundary conditions. The double infinite summations are written to exclude the possibility of both l and m to simultaneously be zero. The power of 2 coefficient, d, will effectively be unity if either l or m is zero and 2 otherwise. However, we have no internal point source or sink. Instead, we can consider the production from the matrix block is for a volume distributed source function that indeed introduces fluid upon pressure decline by expansion. If porosity is uniform, we will have a block that liberates fluid uniformly as the average pressure declines. The Dirichlet solution, however, is not for the pressure relative to the average pressure, but rather the difference in local pressure relative to the boundary pressure. This boundary condition allows fluid passage across the boundary of whatever magnitude necessary to maintain a uniform boundary pressure. We use our degree of freedom to set the boundary pressure to be zero, since all pressures computed are relative. The difference in interpretation of G means we must supply an additional relation to recast the solution in terms of the value relative to the average pressure. Average pressure is always of interest, because it carries material balance information which must be honoured in numerical simulation.

For an area-distributed source, we have

$$G(x,y) = \frac{1}{ab}\int_0^b \int_0^a \frac{4}{\pi^2 ab} \sum_{l,m} \frac{\sin\left(\frac{\pi l x}{a}\right)\sin\left(\frac{\pi m y}{b}\right)\sin\left(\frac{\pi l x_o}{a}\right)\sin\left(\frac{\pi m y_o}{b}\right)}{k_x \frac{l^2}{a^2} + k_y \frac{m^2}{b^2}} dx_o dy_o \tag{5}$$

Dropping anisotropy considerations that can always be reinserted or accounted for in directional stretching, after considerable manipulation, we get per unit area

$$G(x,y)=\frac{1}{2}\left(\frac{b}{a}\right)\left(\frac{y}{b}\right)\left[1-\left(\frac{y}{b}\right)\right]-\frac{4}{\pi^3}\left(\frac{b}{a}\right)\sum_n\frac{sin\left(\frac{\pi(2n-1)y}{b}\right)}{\left[\frac{\pi(2n-1)}{b}\right]^3}\left[\frac{(E_1+E_2-E_3-E_4)}{\left(1-exp\left[-\frac{2\pi(2n-1)a}{b}\right]\right)}\right] \tag{6}$$

with detail left in the Appendix. Here

$$E_1\equiv e^{-\frac{\pi(2n-1)x}{b}};E_2\equiv e^{-\frac{\pi(2n-1)(a-x)}{b}};E_3\equiv e^{-\frac{\pi(2n-1)(a+x)}{b}};E_4\equiv e^{-\frac{\pi(2n-1)(2a-x)}{b}} \tag{7}$$

Using integration to define the average pressure per unit area, we obtain

$$\overline{G}_{SS}=\frac{1}{12}\left(\frac{b}{a}\right)-\frac{8}{\pi^5}\left(\frac{b}{a}\right)^2\sum_{n=1}^{\infty}\frac{1}{(2n-1)^5}\cdot\frac{\left[1-exp\left(-\frac{\pi(2n-1)a}{b}\right)\right]^2}{1-exp\left(-\frac{2\pi(2n-1)a}{b}\right)} \tag{8}$$

2.1.2 Pressure Transient Behaviour

For the full pressure solution, we start with

$$G(x,y;x_o,y_o;t_D)=\frac{4}{\pi^2}\sum_{l,m}\left\{1-e^{-\left[\pi^2\left(\frac{l^2}{a^2}+\frac{m^2}{b^2}\right)t_D\right]}\right\}\frac{sin\left(\frac{\pi lx}{a}\right)sin\left(\frac{\pi my}{b}\right)sin\left(\frac{\pi lx_o}{a}\right)sin\left(\frac{\pi my_o}{b}\right)}{\frac{l^2}{a^2}+\frac{m^2}{b^2}} \tag{9}$$

With some manipulation, we get

$$G(x,y;t)=\frac{b^2}{2}\left(\frac{y}{b}\right)\left[1-\left(\frac{y}{b}\right)\right]-\frac{4}{b}\sum_n\frac{sin\left(\frac{\pi(2n-1)y}{b}\right)}{\left[\frac{\pi(2n-1)}{b}\right]^3}\cdot\frac{E_1+E_2-E_3-E_4}{1-exp\left[-\frac{2\pi(2n-1)a}{b}\right]}-\frac{16}{\pi^4}\sum_{l,m}exp\left[-\pi^2\left(\frac{(2l-1)^2}{a^2}+\frac{(2m-1)^2}{b^2}\right)t_D\right]\cdot\frac{sin\left(\frac{\pi(2l-1)x}{a}\right)sin\left(\frac{\pi(2m-1)y}{b}\right)}{(2l-1)(2m-1)\left(\frac{(2l-1)^2}{a^2}+\frac{(2m-1)^2}{b^2}\right)} \tag{10}$$

which must be evaluated numerically, yet with the benefit of rapidly decaying functions. However, we recognize the contributing terms as the steady state component and a 2D transient summation term.

2.1.3 Average pressure

We developed Eq. 10 for the pressure distribution as a function of time, but we have interest in the average pressure. Performing appropriate spatial integration, we get

$$\overline{G}(t)=\frac{1}{12}\left(\frac{b}{a}\right)-\frac{8}{\pi^5}\left(\frac{b}{a}\right)^2\sum_{n=1}^{\infty}\frac{1}{(2n-1)^5}\left\{\frac{\left[1-e^{-\frac{\pi(2n-1)a}{b}}\right]^2}{1-e^{-\frac{2\pi(2n-1)a}{b}}}\right\}-\frac{64}{\pi^6}\left(\frac{a}{b}\right)\sum_{l,m}\frac{exp\left[-\pi^2\left(\frac{(2l-1)^2}{a^2}+\frac{(2m-1)^2}{b^2}\right)t_D\right]}{(2l-1)^4(2m-1)^2+\left(\frac{a}{b}\right)^2(2l-1)^2(2m-1)^4} \tag{11}$$

2.1.4 Boundary Flux

In the interest in determining the flux distribution of material across different faces of matrix blocks as a function of time, we take the spatial derivative of Eq. 10 to be evaluated at the fracture-matrix boundary. For single phase depletion, this constitutes the exchange function. We get

$$\frac{dG(0,y;t_D)}{dx}=\frac{4b}{\pi^2}\sum_n\frac{n\cdot sin\left(\frac{\pi(2n-1)y}{b}\right)}{(2n-1)^3}\left[\frac{\left(1-e^{-\frac{\pi(2n-1)a}{b}}\right)^2}{\left(1-e^{-\frac{2\pi(2n-1)a}{b}}\right)}\right]-\frac{16a}{\pi^3}\sum_{l,m}\frac{exp\left[-\frac{\pi^2}{a^2}\left((2l-1)^2+\left(\frac{a}{b}\right)^2(2m-1)^2\right)t_D\right]\cdot sin\left(\frac{\pi(2m-1)y}{b}\right)}{(2m-1)(2l-1)^2+\left(\frac{a}{b}\right)^2(2m-1)^3} \tag{12}$$

and

$$\frac{dG(x,0;t_D)}{dy}=\frac{b}{2}-\frac{4}{b}\sum_n\frac{1}{\left[\frac{\pi(2n-1)}{b}\right]^2}\left[\frac{(E_1+E_2-E_3-E_4)}{\left(1-e^{-\frac{2\pi(2n-1)a}{b}}\right)}\right]-\frac{16}{\pi^3 b}\sum_{l,m}exp\left[-\pi^2\left(\frac{(2l-1)^2}{a^2}+\frac{(2m-1)^2}{b^2}\right)t_D\right]\cdot\frac{sin\left(\frac{\pi(2l-1)x}{a}\right)}{(2l-1)\left(\frac{(2l-1)^2}{a^2}+\frac{(2m-1)^2}{b^2}\right)} \tag{13}$$

The total flux across each face can be obtained by integrating along the border yielding

$$\int_0^b \frac{dG(0,y;t_D)}{dx}dy = \frac{8}{\pi^3}\left(\frac{b}{a}\right)\sum_n \frac{n}{(2n-1)^4}\left[\frac{\left(1-e^{-\frac{\pi(2n-1)a}{b}}\right)^2}{\left(1-e^{-\frac{2\pi(2n-1)a}{b}}\right)}\right] - \frac{32}{\pi^4}\sum_{l,m}\frac{exp\left[-\frac{\pi^2}{a^2}\left((2l-1)^2+\left(\frac{a}{b}\right)^2(2m-1)^2\right)t_D\right]}{(2m-1)^2(2l-1)^2+\left(\frac{a}{b}\right)^2(2m-1)^4} \quad (14)$$

and

$$\int_0^a \frac{dG(0,y;t_D)}{dy}dx = \frac{1}{2}-\frac{8}{\pi^3}\left(\frac{b}{a}\right)\sum_n \frac{1}{n(2n-1)^2}\left[\frac{\left(1-e^{-\frac{\pi(2n-1)a}{b}}\right)^2}{\left(1-e^{-\frac{2\pi(2n-1)a}{b}}\right)}\right] - \frac{32}{\pi^4}\sum_{l,m}\frac{exp\left[-\frac{\pi}{a^2}^2\left((2l-1)^2+\frac{a^2}{b^2}(2m-1)^2\right)t_D\right]}{\left(\frac{b}{a}\right)^2(2l-1)^4+(2m-1)^2(2l-1)^2} \quad (15)$$

Thus, for homogenous matrix blocks, we have a nearly complete description of the time dependent depletion process.

2.2 Anisotropic, homogeneous matrix block behaviour without a source

Again, for single phase solutions for pressure, we seek the solution to the 1-D Heat Equation with no internal source

$$\kappa\frac{\partial^2 u}{\partial x^2} = \frac{\partial u}{\partial t} \quad (16)$$

Carslaw and Yeager [18] gave us a 1D solution on a domain, $-a < x < a$, with unit initial value and zero value applied at the boundaries at $t = 0$ as

$$\psi(x,a,t) = \frac{4}{\pi}\sum_{l=0}^{\infty}\frac{(-1)^l}{2l+1}e^{-\frac{k\pi^2}{4a^2}(2l+1)^2 t}\cos\frac{(2l+1)\pi x}{2a} \quad (17)$$

Using the Newman Product Rule [19], we get the following for the area, $-a < x < a, -b < y < b$.

$$\psi(x,y,a,b,t) = \frac{16}{\pi^2}\sum_{l,m=0}^{\infty}\frac{(-1)^{l+m}e^{-\frac{\pi^2}{4}\left[\frac{k_x}{a^2}(2l+1)^2+\frac{k_y}{b^2}(2m+1)^2\right]t}}{(2l+1)(2m+1)}cos\left[\frac{\pi}{2}(2l+1)\left(\frac{x}{a}\right)\right]cos\left[\frac{\pi}{2}(2m+1)\left(\frac{y}{b}\right)\right] \quad (18)$$

In this formulation with no source, the block "bleeds" into the fracture. A transient pulse migrates towards the center of mass, followed by a depletion of the block average pressure towards a steady state of zero everywhere. The time dependent block pressure then follows

$$\overline{\psi}(a,b,t) = \frac{64}{\pi^4}\sum_{l,m=0}^{\infty}\frac{e^{-\frac{\pi^2}{4}\left[\frac{k_x}{a^2}(2l+1)^2+\frac{k_y}{b^2}(2m+1)^2\right]t}}{(2l+1)^2(2m+1)^2} \quad (19)$$

We can likewise probe the exuding flux distributions at the boundaries with

$$\frac{d\psi(a,y,a,b,t)}{dx} = \frac{8}{a\pi}\sum_{l,m=0}^{\infty}\frac{(-1)^{1+2l+m}}{(2m+1)}\cos\left[\frac{\pi}{2}(2m+1)\left(\frac{y}{b}\right)\right]e^{-\frac{\pi^2}{4}\left[\frac{k_x}{a^2}(2l+1)^2+\frac{k_y}{b^2}(2m+1)^2\right]t} \quad (20)$$

and

$$\frac{d\psi(x,b,a,b,t)}{dy} = \frac{8}{\pi b}\sum_{l,m=0}^{\infty}\frac{(-1)^{1+l+2m}}{(2l+1)}\cos\left[\frac{\pi}{2}(2l+1)\left(\frac{x}{a}\right)\right]e^{-\frac{\pi^2}{4}\left[\frac{k_x}{a^2}(2l+1)^2+\frac{k_y}{b^2}(2m+1)^2\right]t} \quad (21)$$

or the total flux at respective boundaries as

$$\int_{-b}^{b}\frac{d\psi(a,y,a,b,t)}{dx}dy = -\frac{32}{\pi^2}\left(\frac{b}{a}\right)\sum_{l,m=0}^{\infty}\frac{e^{-\frac{\pi^2}{4}\left[\frac{k_x}{a^2}(2l+1)^2+\frac{k_y}{b^2}(2m+1)^2\right]t}}{(2m+1)^2} \quad (22)$$

and

$$\int_{-a}^{a} \frac{d\psi(x,b,a,b,t)}{dy} dx = -\frac{32}{\pi^2}\left(\frac{a}{b}\right)\sum_{l,m=0}^{\infty} \frac{e^{-\frac{\pi^2}{4}\left[\frac{k_x}{a^2}(2l+1)^2+\frac{k_y}{b^2}(2m+1)^2\right]t}}{(2l+1)^2} \quad (23)$$

This gives a substantially different behaviour and one more in alignment with discovery of a primary fracture system dividing the medium into discontinuous matrix blocks, each progressively emptying their contents into a constant pressure sink.

2.3 Matrix embedded fracture model development

For an internal line source starting at (x_1,y_1) parameterized in s using direction cosines, α and β, we have

$$G(x,y;t_D) = \frac{4}{\pi^2}\int_0^1 \sum_{l,m}\left\{1-e^{-\pi^2\left(\frac{k_x l^2}{a^2}+\frac{k_y m^2}{b^2}\right)t_D}\right\} \cdot \frac{\sin\left(\frac{\pi l x}{a}\right)\sin\left(\frac{\pi m y}{b}\right)\sin\left(\frac{\pi l(x_1+\alpha s)}{a}\right)\sin\left(\frac{\pi m(y_1+\beta s)}{b}\right)}{k_x\frac{l^2}{a^2}+k_y\frac{m^2}{b^2}} ds \quad (24)$$

We can divide this into time independent and dependent contributions.

$$G(x,y,t_D) = G_o(x,y) - G_{2D}(x,y,t_D) \quad (25)$$

The pseudo-steady state line source solution is a quite complicated development with significant singularity handling. The analogous development of Hazlett and Babu (2014) suitably modified for Dirichlet boundary conditions is required. The transient terms are given by

$$G_{2D}(x,y;t_D) = \frac{4a^2}{\pi^3 k_x}\sum_{l,m}\frac{\sin\left(\frac{\pi l x}{a}\right)\sin\left(\frac{\pi m y}{b}\right)}{l^2+m^2\left(\frac{k_y}{k_x}\right)\left(\frac{a}{b}\right)^2} exp\left[-\pi^2\left(\frac{k_x}{a^2}\right)\left[l^2+m^2\left(\frac{k_y}{k_x}\right)\left(\frac{a}{b}\right)^2\right]t_D\right] \cdot \left\{\begin{array}{c}\left(\frac{ab}{l\alpha b - m\beta a}\right)cos\left[\pi\left(\frac{lx_m}{a}-\frac{my_m}{b}\right)\right]sin\left[\pi\left(\frac{lx_d}{a}-\frac{my_d}{b}\right)\right] \\ -\left(\frac{ab}{l\alpha b + m\beta a}\right)cos\left[\pi\left(\frac{lx_m}{a}+\frac{my_m}{b}\right)\right]sin\left[\pi\left[\left(\frac{lx_d}{a}+\frac{my_d}{b}\right)\right]\right]\end{array}\right\} \quad (26)$$

where

$$x_m = \frac{x_2+x_1}{2}, y_m = \frac{y_2+y_1}{2}, x_d = \frac{x_2-x_1}{2}, y_d = \frac{y_2-y_1}{2}, x_2 = x_1+\alpha, y_2 = y_1+\beta \quad (27)$$

In this formulation, in the limit, $t_D \rightarrow 0$, the transient solution exactly cancels the steady state contribution to give back the no change from a zero initial condition state for any observation point (x,y).

2.4 Manifestation of microfractures on macroscopic properties

We examine the scaleup of samples containing microfractures in 2D by treating the fractures as infinite conductivity linear features. Using superposition, we utilize the solution for a single fracture to multiple fractures, whether these be isolated or single fracture segments. For one fracture, the Neumann or Green's function development was for a uniform flux segment. Since one cannot fix both pressure and flux, there exists a pressure distribution along a uniform flux line segment. This problem can be converted to uniform pressure through segmentation and solving for the flux distribution that would give the same pressure at a fixed number of control points. The sum of fluxes must be equal to the constant rate specified. Here we choose to specify that rate to be zero. Thus, we solve for a net-zero flux condition yielding uniform pressure at control points along the fracture, chosen to be at segment midpoints. The problem can readily be generalized to multiple fractures via superposition. This procedure is illustrated in Fig. 1 for segmentation of a simple linear fracture into 10 elements. Note that we choose to use geometric segmentation from the midpoint outwards in order to capture the effect of fracture tips. If one chooses a geometric ratio (R) and a number of segments (n_s), the endpoints of each segment are determined. For a

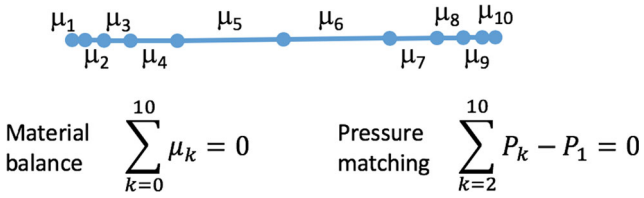

Fig. 1 Construction of net-zero flux, uniform pressure fractures through segmentation, material balance, and pressure matching constraints. We choose a reference pressure, here P_1, to constrain fluxes. A sparse iterative solver (GMRES) is used to compute the segment flux distributions, μ_k

segment of length L and $n_s = 10$, we have $L_2 = R^*L_1$, $L_3 = R^*L_2$, $L_4 = R^*L_3$, $L_5 = R^*L_4$, and the constraint $\sum_1^5 L_i = \frac{L}{2}$. Thus,

$$L_1 = \frac{L}{2}\left(\frac{1}{\sum_{j=1}^{n_s/2} R^{j-1}}\right) \tag{28}$$

Furthermore, $n_s = 10$ and R = 1.5 were found sufficient to resolve flux distribution through comparison of profiles with more refined discretization, yet greater computational load.

We systematically study the effect of microfracture density and orientation on single phase macroscopic transport properties making use of both Neumann and Dirichlet boundaries. In particular, we set up a flow field of uniform matrix properties with single and multiple oriented net-zero flux line segments. While, in principle, line segments can intersect to create internal complex fractures and fracture swarms, our initial automated procedure was not set up with automatic cluster analysis to identify fracture sets which should be treated as distinct constant pressure features. An alternate approach would be to enter interconnected fracture systems as associated entities and enforce constant pressure throughout. The role of fracture intersections and swarms is left for future investigation, but characterization of the input represents yet another level of complexity. Instead, we used random generation of fracture segments of specified length and/or orientation and excluded processing of intersecting fractures. On the generated flow field, we have the general Neumann problem with zero flux on the lateral edges and uniform flux at the inlet and outlet face. This is the general configuration for coreflood performance. The geometry is mirrored, yielding a constant pressure boundary condition along the central slice. Thus, the impact of simulated internal microfractures is examined along the central line of symmetry with respect to effective transport properties in the direction of flow and induced flow in the direction normal to flow due to the subscale heterogeneity.

3 Results and discussion

Figure 2 shows depictions of the steady state pressure distribution in blocks of different aspect ratios according to Eq. 6. As a further demonstration, Fig. 3 gives transient pressure distributions for a 2:1 aspect ratio rectangle according to Eq. 10. The steady state average pressure and the corresponding productivity index as a function of aspect ratio is provided in Fig. 4, along with the evolution of $\overline{P} - P_{boundary}$ for three different isotropic matrix block shapes. Recall, these can also represent permeability scaled shapes in the case of anisotropic media. We see the transient behaviour of matrix blocks leading to a pseudo-steady state where the spatial gradients in pressure are no longer functions of time. We model the average pressure in the matrix block – something not amenable to measurement, but which does carry material balance information. Note this is different from traditional well testing for naturally fractured reservoirs where the well is responding to the dynamics of interaction with the primary fracture set that is, in turn, interacting with matrix. A well intersecting an infinite conductivity fracture would distribute the observed pressure deeper into the matrix, which surely influences the system performance. However, the average pressure forecast seen here is connected to the rate of recovery rather than the pressure at a discrete observation point.

The case of the square drainage block is relevant, but less interesting, as there is no difference between drainage faces. As we progress to larger aspect ratio block, however, we see quite interesting phenomena. At short times, all interface

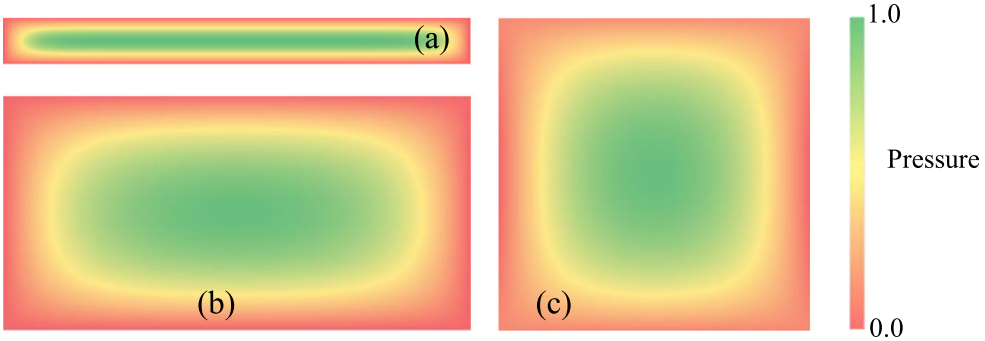

Fig. 2 Steady state pressure distributions in rectangles with uniformly distributed sources and Dirichlet external boundary conditions. (**a**) b:a = 0.1, (**b**) b:a = 0.5, and (**c**) b:a = 1

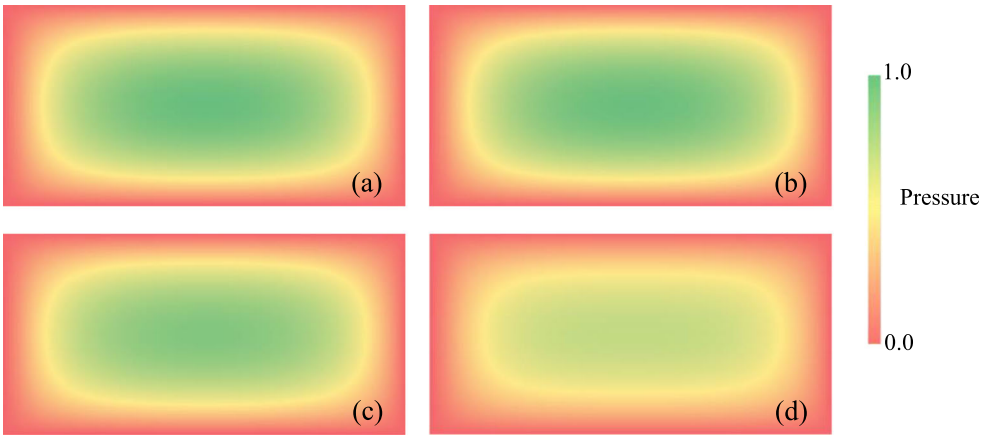

Fig. 3 Dynamic pressure distributions in a 2:1 rectangle with a uniformly distributed source and Dirichlet external boundary conditions as a function of dimensionless time. (**a**) t_D = 1.0, (**b**) tD = 0.1, (**c**) tD = 0.05, and (**d**) tD = 0.025

elements are essentially identical. The influence of pressure gradient is confined to short distances. As depletion continues, there is a significant rise in asymmetry of drainage with longer block faces accounting for an increasing proportion of fluid production. Fluid has less distance to travel normal to the long edge. Once the pressure pulse reaches the centerline, we find fixed, larger pressure gradients in one direction. The bias for directional production persists even in steady state.

Quantitative examination of the flux bias through time is portrayed in Fig. 5a, while the actual distribution of escaping fluid from the rectangle sides is captured in Fig. 5b. Flux follows surface area distribution at very early time, but in late time, a disproportionate share of fluid exits the longer leg. The square, of course, shows no bias throughout all time. In steady state, the sum of the two normalized fluxes on adjacent legs must equal half of the steady state fluid production from a unit area distributed source, i.e. 0.5. Note that the distribution on the short leg is essentially parabolic, but distribution on the longer leg has a blunt nose. Neither is uniform flux. This is relevant to the depiction of average values in order to preserve material balance. Average values may be far from representing the actual distribution of fluid movement from block to block, or in this case, block to fracture.

For matrix blocks in pure depletion mode into surrounding fractures considered as constant pressure sinks, we achieve typical transient pressure distributions, as shown in Fig. 6. There we see a steep pressure gradient resulting from a step change in boundary pressure invading the medium, followed by a decay in towards the steady state of complete depletion. In Fig. 7, we see the ever declining average reservoir pressure, easily related to cumulative production, as a function of aspect ratio.

Moving beyond homogeneous block results, studies in the scaleup of media with internal infinite conductivity features were performed with the geometry and boundary conditions illustrated in Fig. 8 along with an example computation of the pressure field for a system of 25 randomly distributed, randomly oriented microfractures. Every fracture depicted was broken into 10 segments to resolve a flux distribution yielding uniform pressure at segment midpoints, as described previously. These are steady state single phase tests that require the matrix to have some permeability. As seen in Fig. 8, the

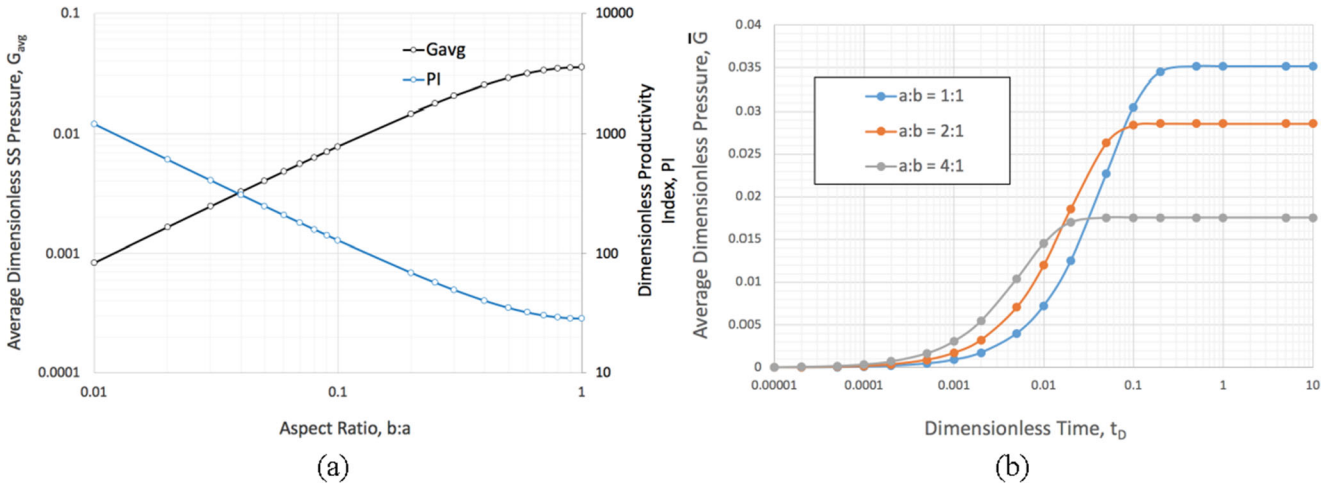

Fig. 4 Average dimensionless pressure relations (**a**) steady state and productivity index (PI) as a function of rectangle aspect ratio, b:a, and (**b**) Block average pressure difference relative to the boundary pressure as a function of time for three block aspect ratios, a:b = (4, 2, 1)

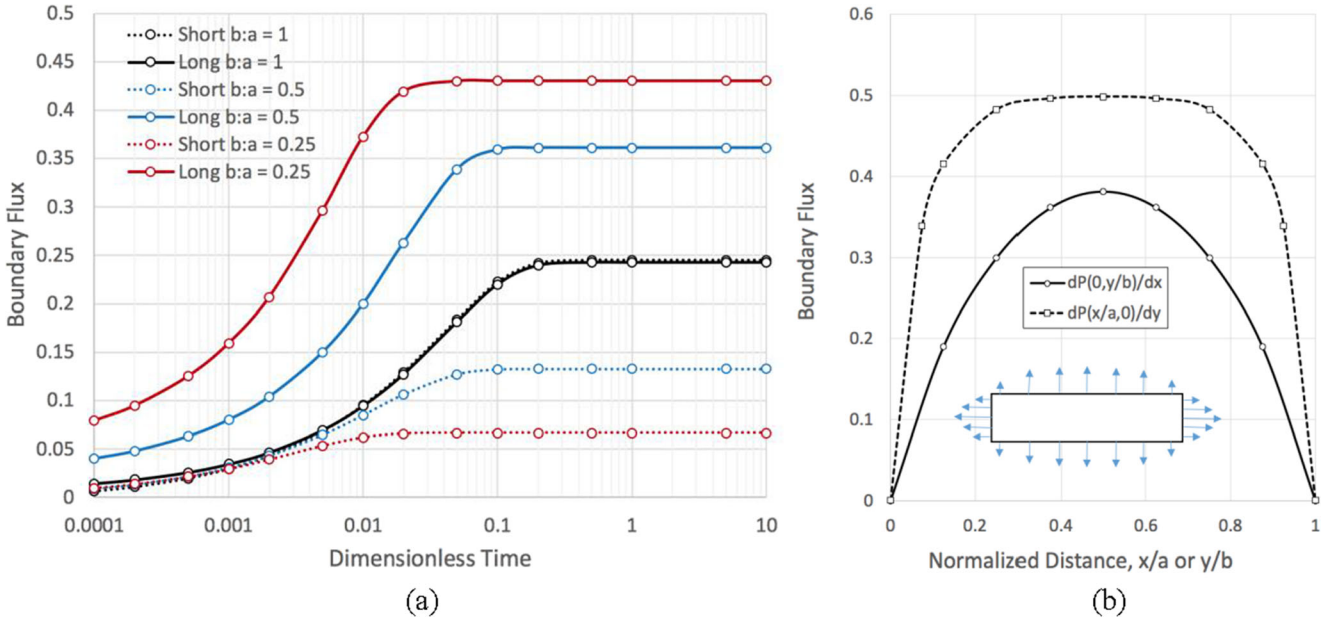

Fig. 5 Integrated boundary flux evolution with time and its steady state distribution. (**a**) Instantaneous total boundary flux by side in rectangles with uniformly distributed sources and Dirichlet external boundary conditions for b:a = 0.25, b:a = 0.5, and b:a = 1, and (**b**) Steady state flux profile from each endface for b:a = 0.25

influence of microfractures is localized and is not as impactful on longer range flow as intuitively believed. Solutions based upon Darcy's Law require that all space be utilized. Only a portion of the flow is admitted into the fracture as a "superhighway." Still, unsteady state distributions may differ and show more impact of internal features, though this was untested here. On the other hand, Fig. 9 shows a much larger uniform pressure internal feature relative to the flow field that significantly influences the effective permeability of the composite medium.

The results of this study are outlined in Tables 1 and 2 and Figs. 10, 11, 12, and 13. Table 1 gives summary results for single fracture tests, while Table 2 gives those for multiple fracture experiments. The geometries for single fracture and multiple fracture test cases are given in Figs. 10 and 12, along with a depiction of the flux distribution along the central uniform pressure boundary. Figs. 11 and 13 give the 1-D depiction of pressure and pressure gradient profiles. Recall $a = 1$ in these scaled numerical experiments, and the simulations were performed on a square sample and its mirror image to yield a constant pressure condition at the midline with uniform flux at the inlet. With the normalized parameterization, steady flow requires the average flux at the midpoint to be unity to match the inlet condition. However, the microfractures, evidenced as constant pressure streaks, introduce bias in the flow field orthogonal to the direction of flow. Thus, we see positive and negative deviations from unit flux in the y-direction. Internally, we see flow in the y-direction induced by introduced heterogeneities. Thus, we can compute the change in effective permeability relative to a homogeneous matrix permeability and quantify the result of permeability as a tensorial property. In Figs. 11a and 13a, a constant slope in the pressure profile represents flow in the homogeneous matrix. Any deviations are a result of the internal infinite conductivity microfracture disturbance of the flow field. In Figs. 11b and 13b, we see the computed pressure gradients, with a slope of −1 indicative of the homogeneous matrix in this dimensionless system. Note that microfractures result in a lowering of the magnitude of the slope locally and in an averaged sense. This allows direct assignment of effective permeability relative to that of a homogeneous matrix. Orientation, continuity, and effective length are all seen as important in defining effective properties.

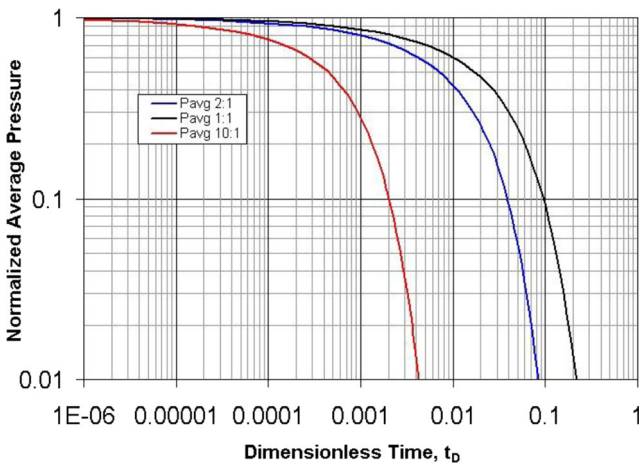

Fig. 6 Normalized pressure versus time for blocks of various aspect ratios for depletion into the surrounding constant pressure fracture system, a = k_x = 1

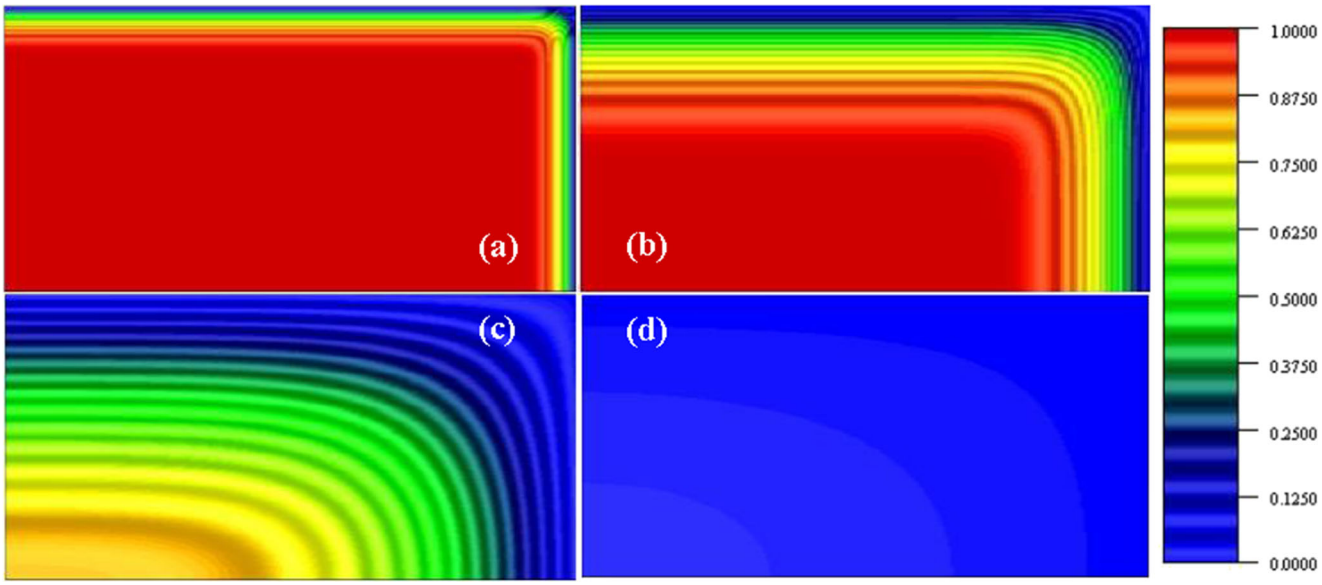

Fig. 7 Evolving pressure distribution in a block with aspect ratio a:b = 2 with depletion into the surrounding constant pressure fracture system, a = k_x = 1, showing only the first quadrant

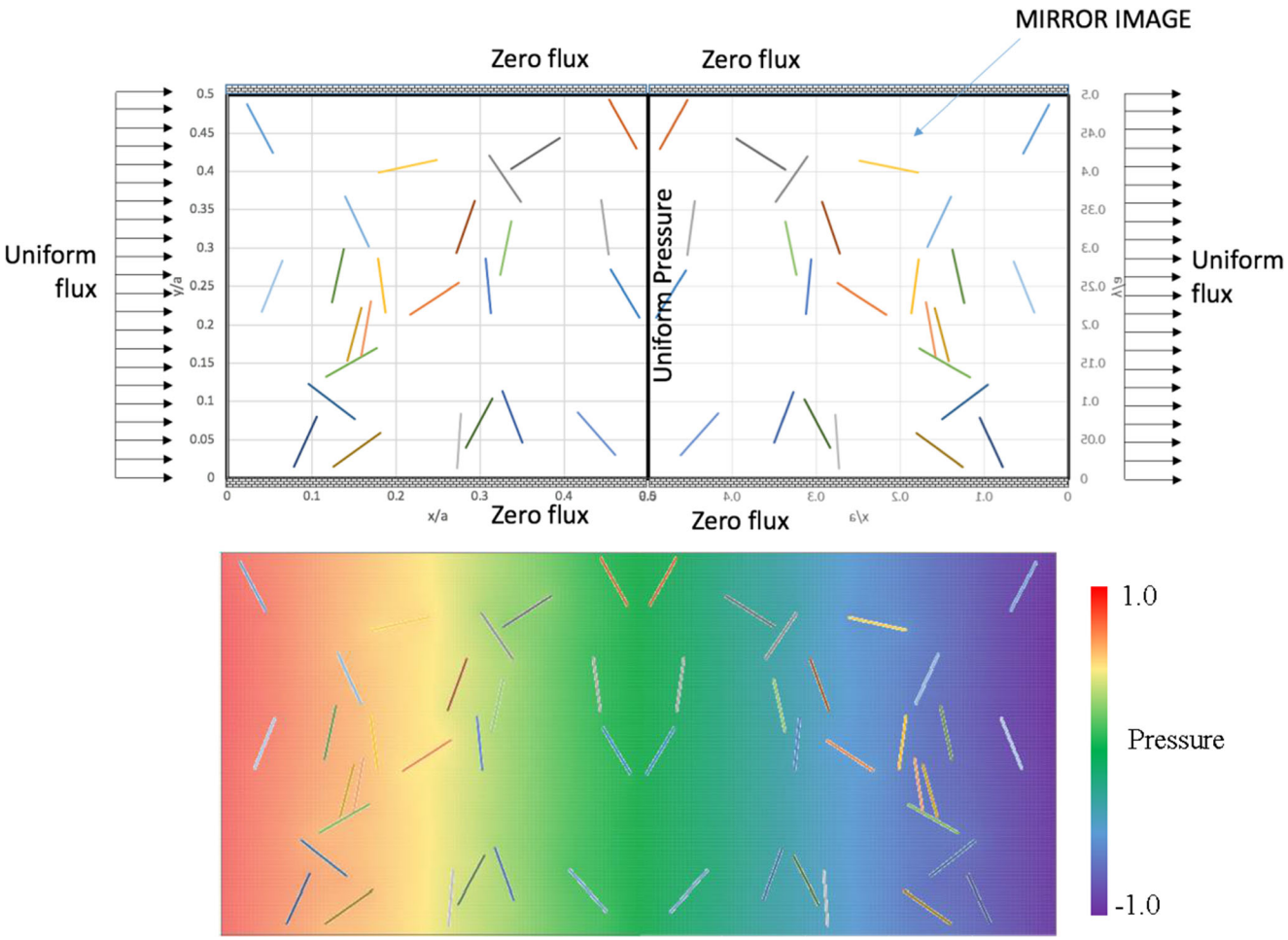

Fig. 8 Pressure distribution for steady single phase flow from left to right with uniform flux external boundaries and 25 superimposed randomly oriented infinite conductivity features (15%) and their mirror images. The pressure distribution appears to be only mildly impacted by the size of these features without preferred orientation despite their relatively high density. Fractures are shown as superimposed coloured line segments for visualization purposes only and do not reflect pressure

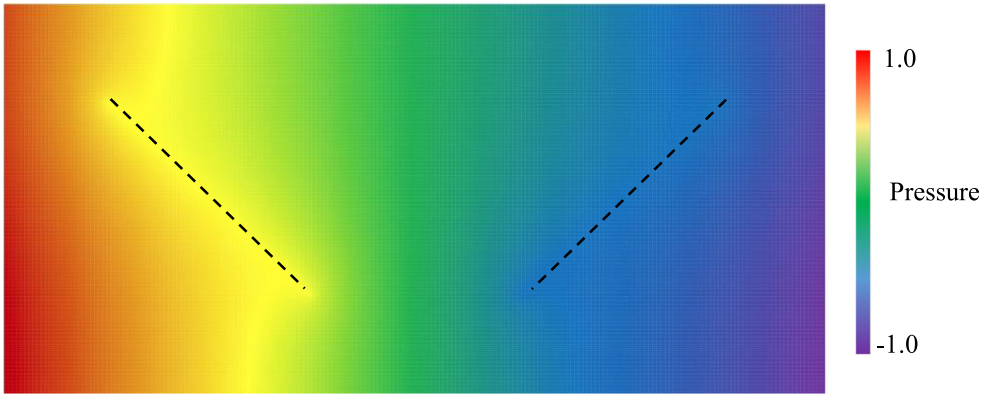

Fig. 9 Pressure distribution for steady single phase flow from left to right with uniform flux external boundaries and a diagonal infinite conductivity feature (in yellow) and its less visible mirror image in blue. This construction yields a constant pressure (Dirichlet) central boundary for studying the impact of internal heterogeneities on the flow field and macroscopic transport properties. Fracture positions are shown by the superimposed dotted lines

When microfractures are less than 10% of the characteristic length scale of a flow measurement, there is negligible impact regardless of orientation or frequency. The maximum impact on permeability in the direction of flow, k_x, of all tests performed was only 33%. Fracture intersections are not anticipated to change these results which are moderated by the relative size of heterogeneities with respect to the flow field. In large flow systems, the influence of small scale features is highly localized. Should cluster sizes grow to a significant degree, they would carry significant influence. In these studies, microfractures aligned normal to the flow direction have no impact in steady, single phase, 1-D flow, while those parallel to flow direction have maximum effect. In multi-dimensional or multiphase flows, the presence of fractures even normal to the flow may have an impact due to their ability to redistribute flow.

Note that the permeability is computed for 1D flow with imposed 2D heterogeneity. With the test geometry, we can evaluate flow bias in the y-direction due to pressure drop imputed in the x-direction. The resulting flow field gives tensorial permeability information introduced by underlying microstructure.

The flow field is strongly biased by heterogeneities near the outlet boundary. Those touching the outlet dramatically bias

Table 1 Scale-up results for single microfractures in matrix

CASE	Feature Length, L/a	x_1	y_1	x_2	y_2	Orientation Angle, θ	Permeability Change, %	$\frac{d}{dy}\left(\frac{dP}{dx}\right)$
A	0.354	0	0	0.25	0.25	45	12	0.2
B	0.354	0	0.125	0.25	0.375	45	14	0.575
C	0.354	0.125	0.125	0.375	0.375	45	17	1.25
D	0.354	0.25	0.125	0.5	0.375	45	25	3.34
E	0.354	0.073	0.25	0.427	0.25	0	33	0
F	0.354	0.25	0.073	0.25	0.427	90	0	0
G	0.354	0.097	0.162	0.403	0.338	30	26	1.21
H	0.354	0.162	0.097	0.338	0.403	60	9	0.962

Table 2 Scale-up results for multiple microfractures in matrix

CASE	Total Fracture Length, L/a	Number of Fractures	Orientation Angle, θ	Permeability Change, %	$\frac{d}{dy}\left(\frac{dP}{dx}\right)$
I	0.354	10	45	2	0.066
J	0.354	10	45	2	0.105
K	0.354	25	45	5	0.228
L	0.354	25	45	5	0.227
M	0.707	25	45	16	1.37
N	0.707	25	0	31	0.59
O	0.707	25	random	10	−0.375
P	0.707	25	random	18.2	−0.292

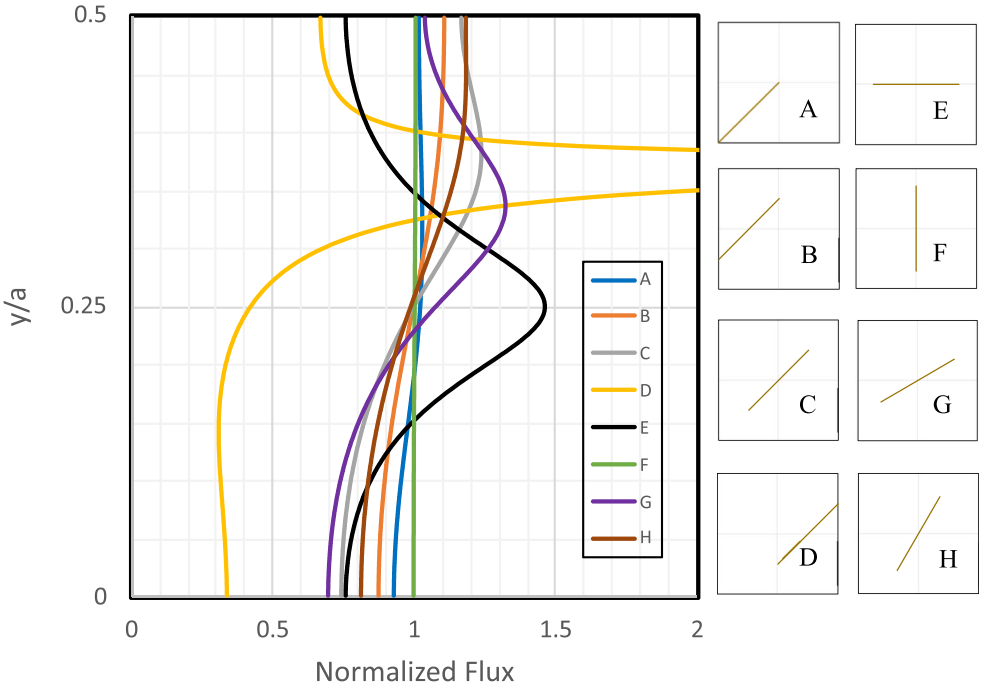

Fig. 10 Scale-up cases for single microfractures in matrix: Geometry and resulting outlet flux profile

flow. Randomly oriented microfractures have an impact on effective permeability, but they do not introduce tensorial permeability effects for truly random orientations. Features normal to the flow direction also do not introduce flow bias in the y-direction.

Note that we excluded the influence of interconnected fracture swarms. With the knowledge that in steady state such features will behave as an enlarged, single, oriented oval feature [15], we can infer magnitude of impact. Additional testing is warranted to quantify such effects. With extraordinarily low matrix permeability, the flow field may be dominated by transients rather than steady state behaviour. With zero matrix permeability, we rely on percolation of the fracture microfabric. Such behaviour can be modelling within the context of similar studies only with finite permeability fracture networks and a modified set of equations that replace the pressure matching expressions of Fig. 1.

4 Conclusions

Pseudo-steady state and time dependent Green's function solutions were produced for depletion from homogenous, anisotropic matrix blocks in two dimensions with an area-distributed source. These solutions were spatially averaged to produce driving force expressions for matrix blocks drained by a prevailing primary fracture system. Additionally, boundary flux expressions were derived to indicate the anisotropic

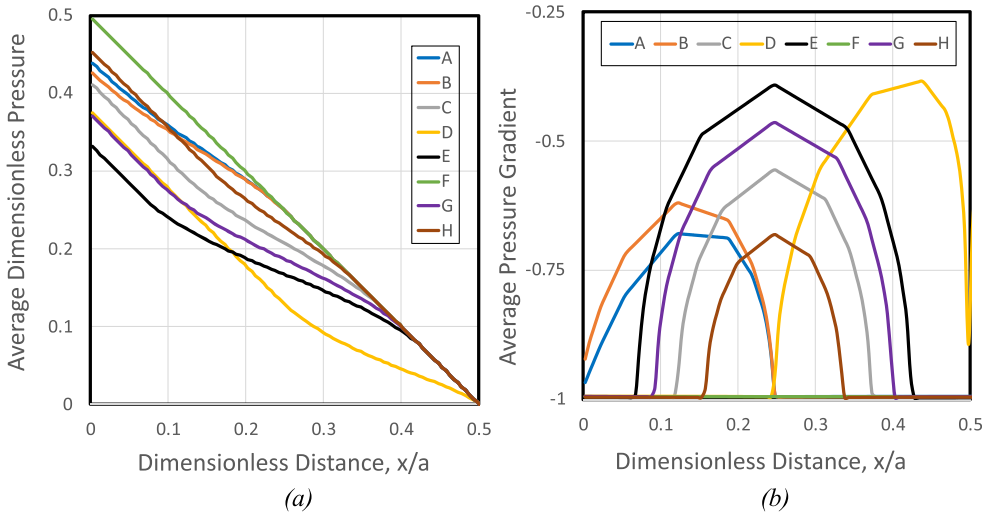

Fig. 11 Scale-up cases for single microfractures in matrix: (**a**) Averaged (1-D) pressure normal to flow verses distance through the sample, and (**b**) Averaged (1-D) pressure gradient normal to flow verses distance through the sample

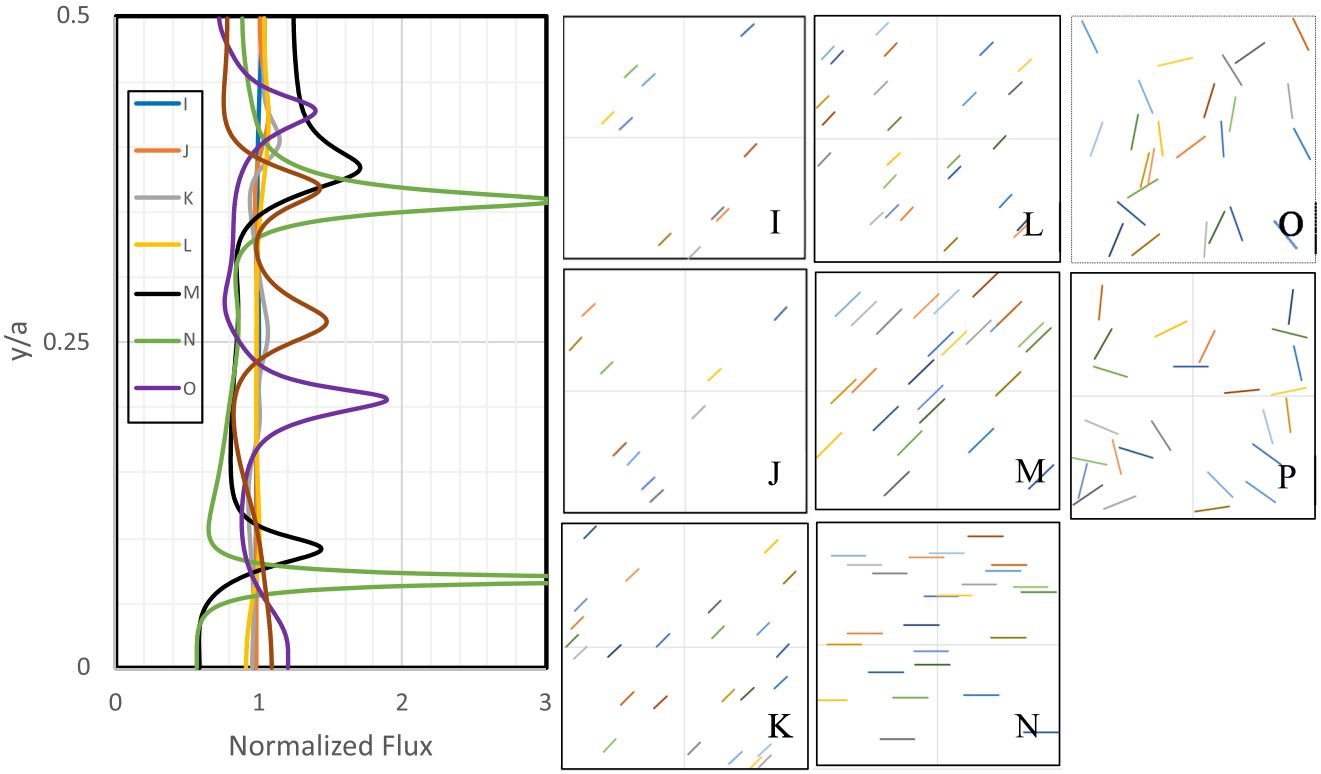

Fig. 12 Scale-up cases for multiple microfractures in matrix: Geometry and resulting outlet flux profile

nature of block depletion. If the internal source is excluded, we get a different picture of a matrix block in depletion mode into a surrounding fracture system of constant pressure. In this case, the average pressure shows two regimes: one in which the pressure disturbance propagates towards the center of mass, and a second with progressive reduction of the smooth pressure distribution towards complete depletion. The model was extended to a block containing a uniform flux single, arbitrarily-oriented fracture with Dirichlet external boundaries. Through superposition, such models were demonstrated to be readily generalized to discrete, uniform pressure features internal to the matrix block. Many single and multiple microfracture case studies were conducted to ascertain the impact of subscale fractures on macroscopic properties with scale-up implications.

The pressure driving force was found to be a strong function of block shape during both transient and pseudo-steady state flow regimes. While the pressure at fixed observation point follows diffusive behaviour characterized by Bourdet derivative slopes of ½ in pressure transient analysis, the

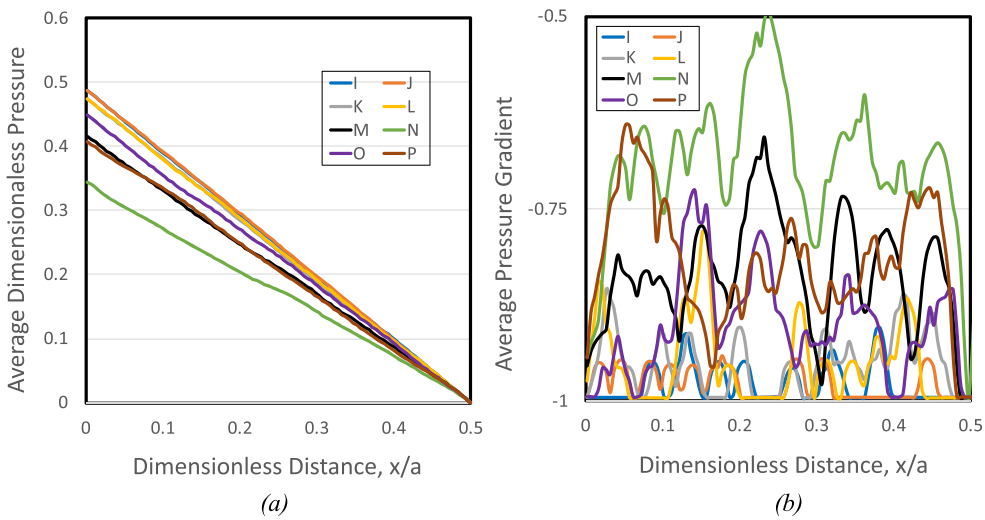

Fig. 13 Scale-up cases for multiple microfractures in matrix: (**a**) Averaged (1-D) pressure normal to flow verses distance through the sample, and (**b**) Averaged (1-D) pressure gradient normal to flow verses distance through the sample

average driving force shows a slope of unity (−1 in terms of its inverse, productivity index). Production from blocks was found to be anisotropic with regard to drainage face and disproportionate to area of contact. Furthermore, flux distribution was examined and found to depart dramatically from uniform flux, with implications in numerical simulation using only average values.

Without an embedded source term, we observe a continuous decline in average reservoir pressure with a dependence upon aspect ratio. The initial and final boundary flux ratios reflect the relative length of boundaries with intermediate values showing the competition of moving gradients towards respective lines of symmetry, the intersection of which defines the center of mass. With such a model, we are able to characterize the dynamic behaviour of single phase depletion in homogeneous 2D rectangularly blocks of arbitrary aspect ratio surrounded by infinite conductivity fractures analytically and completely.

A novel flow experiment was designed that allowed an analytic solution of single phase steady flow in a heterogeneous system of matrix and discrete infinite conductivity fractures. This included the ability to extract imputed tensorial permeability properties due to microfabric orientation. Fracture orientation, continuity, density, and effective length were all important in defining effective properties, yet the overall impact was much less dramatic than anticipated due to the space-filling nature of flow required by Darcy's Law at steady state. The presence of large permeability features disturbs the flow field locally, but does not allow for large-scale diversion of flow at the exclusion of flow through matrix. The maximum impact on permeability of a single fracture or set of microfractures within the limited size and density sets examined was a 33% change in k_x.

These results constitute major building blocks in forward plans to entertain block size distributions and advanced numerical schemes with underlying analytical constructs. Additional experiments are warranted to examine transient effects with internal fractures, finite conductivity fractures, and fracture swarms to further quantify the impact of oriented microfracture fabric on effective macroscopic properties. The model can be further generalized to 3D and arbitrarily-oriented, partially penetrating fractures following the work of Bao et al. [21] extended to Dirichlet boundary conditions.

Appendix

Block Pressure Distribution, $G(x,y) = P(x,y) - P_{boundary}$.

Integrating Eq. 3 and separating terms, we get

$$G(x,y) = \frac{4a}{\pi^4 b}\sum_m \frac{[1-cos(\pi m)]sin\left(\frac{\pi m y}{b}\right)}{m} \cdot \sum_{l=1} \frac{sin\left(\frac{\pi l x}{a}\right)[1-cos(\pi l)]}{l\left(l^2+\frac{a^2}{b^2}m^2\right)} \tag{A1}$$

From Gradshtein and Ryzhik [22], we have the following identities.

$$\sum_{k=1} \frac{cos\left(\frac{\pi k x}{a}\right)}{k^2+\beta^2} = \left(\frac{\pi}{2\beta}\right)\frac{cosh\left[\pi\beta\left(1-\frac{x}{a}\right)\right]}{sinh(\pi\beta)} - \frac{1}{2\beta^2} \tag{A2}$$

and

$$\sum_{k=1} \frac{(-1)^k cos\left(\frac{\pi k x}{a}\right)}{k^2+\beta^2} = \left(\frac{\pi}{2\beta}\right)\frac{cosh\left(\frac{\pi\beta x}{a}\right)}{sinh(\pi\beta)} - \frac{1}{2\beta^2} \tag{A3}$$

Subtracting these and noting we can write $(-1)^k$ as cos(πk),

$$\sum_{k=1} \frac{cos\left(\frac{\pi k x}{a}\right)[1-cos(\pi k)]}{k^2+\beta^2} = \left(\frac{\pi}{2\beta}\right)\frac{cosh\left[\pi\beta\left(1-\frac{x}{a}\right)\right] - cosh\left(\frac{\pi\beta x}{a}\right)}{sinh(\pi\beta)} \tag{A4}$$

Integrating with respect to x from zero to x and simplifying, we get

$$\sum_{k=1} \frac{[1-cos(\pi k)]sin\left(\frac{\pi k x}{a}\right)}{k\left(k^2+\beta^2\right)} = \left(\frac{\pi}{2\beta^2}\right)\frac{sinh(\pi\beta) - \left[sinh\left[\pi\beta\left(1-\frac{x}{a}\right)\right] + sinh\left(\frac{\pi\beta x}{a}\right)\right]}{sinh(\pi\beta)} \tag{A5}$$

Substituting for k and β,

$$\sum_{l=1}\frac{[1-cos(\pi l)]sin\left(\frac{\pi lx}{a}\right)}{l\left(l^2+\left(\frac{ma}{b}\right)^2\right)} = \frac{\pi}{2}\left(\frac{b}{ma}\right)^2\frac{sinh\left(\pi\left(\frac{ma}{b}\right)\right)-\left[sinh\left[\pi\left(\frac{ma}{b}\right)\left(1-\frac{x}{a}\right)\right]+sinh\left(\frac{\pi\left(\frac{ma}{b}\right)x}{a}\right)\right]}{sinh\left(\pi\left(\frac{ma}{b}\right)\right)} \tag{A6}$$

Applying this new identity to Eq. A1, after some rearrangement, we get

$$G(x,y) = \frac{2b}{\pi^3 a}\sum_m\frac{[1-cos(\pi m)]sin\left(\frac{\pi my}{b}\right)}{m^3}\left\{1-\frac{\left[sinh\left[\left(\frac{\pi m}{b}\right)(a-x)\right]+sinh\left(\frac{\pi mx}{b}\right)\right]}{sinh\left(\frac{\pi ma}{b}\right)}\right\} \tag{A7}$$

Substituting hyperbolics for their exponential counterparts,

$$G(x,y) = \frac{2b}{\pi^3 a}\sum_m\frac{[1-(-1)^m]sin\left(\frac{\pi my}{b}\right)}{m^3}\left\{1-\left[\frac{e^{\frac{\pi m(x-a)}{b}}-e^{-\frac{\pi m(x+a)}{b}}+e^{-\frac{\pi mx}{b}}-e^{-\frac{\pi m(2a-x)}{b}}}{1-e^{-\frac{2\pi ma}{b}}}\right]\right\} \tag{A8}$$

Since only odd terms will contribute and yield a coefficient of 2,

$$G(x,y) = \frac{4b}{\pi^3 a}\sum_{n=1}^{\infty}\frac{sin\left(\frac{\pi(2n-1)y}{b}\right)}{(2n-1)^3}\left[1-\frac{(E_1+E_2-E_3-E_4)}{\left(1-e^{-\frac{2\pi(2n-1)a}{b}}\right)}\right] \tag{A9}$$

where E_j terms are defined in Eq. 7. The leading term can be analytically reduced using the derived identity

$$\sum_k\frac{(-1)^k sin(kx)}{k^3} = \frac{x}{12}\left(x^2-\pi^2\right) \tag{A10}$$

Substitution yields Eq. 6 in the text.

Block Average Pressure Difference, $\overline{G} = \overline{P} - P_{boundary}$.
Applying the definition of an average to Eq. 6,

$$\overline{G}_{SS} = \frac{1}{ab}\frac{b}{a}\int_0^a\int_0^b\left\{\frac{b^2}{2}\left(\frac{y}{b}\right)\left[1-\left(\frac{y}{b}\right)\right]-\frac{4}{b}\sum_n\frac{sin\left(\frac{\pi(2n-1)y}{b}\right)}{\left[\frac{\pi(2n-1)}{b}\right]^3}\left[\frac{(E_1+E_2-E_3-E_4)}{\left(1-e^{-\frac{2\pi(2n-1)a}{b}}\right)}\right]\right\}dy\,dx \tag{A11}$$

After one integration, we get

$$\overline{G}_{SS} = \frac{1}{ab}\int_0^b\left\{\frac{b^2}{2}\left(\frac{y}{b}\right)\left[1-\left(\frac{y}{b}\right)\right]x-\frac{4}{b}\sum_{n=1}^{\infty}\frac{sin\left(\frac{\pi(2n-1)y}{b}\right)}{\left[\frac{\pi(2n-1)}{b}\right]^3}\left[\frac{I_1+I_2-I_3-I_4}{1-e^{-\frac{2\pi(2n-1)a}{b}}}\right]\right\}_0^a dy \tag{A12}$$

with

$$I_1\equiv-\left[\frac{b}{\pi(2n-1)}\right]e^{-\frac{\pi(2n-1)x}{b}};\ I_2\equiv\left[\frac{b}{\pi(2n-1)}\right]e^{-\frac{\pi(2n-1)(a-x)}{b}};$$
$$I_3\equiv\left[-\frac{b}{\pi(2n-1)}\right]e^{-\frac{\pi(2n-1)(a+x)}{b}};\ I_4\equiv\left[\frac{b}{\pi(2n-1)}\right]e^{-\frac{\pi(2n-1)(2a-x)}{b}}, \tag{A13}$$

which reduces to

$$\overline{G}_{SS} = \frac{1}{b}\int_0^b\left\{\frac{b^2}{2}\left(\frac{y}{b}\right)\left[1-\left(\frac{y}{b}\right)\right]\right\}dy-\frac{1}{ab}\int_0^b\left\{\frac{4}{b}\sum_{n=1}^{\infty}\frac{sin\left(\frac{\pi(2n-1)y}{b}\right)}{\left[\frac{\pi(2n-1)}{b}\right]^4}\left[\frac{\left[1-e^{-\frac{\pi(2n-1)a}{b}}\right]^2}{1-e^{-\frac{2\pi(2n-1)a}{b}}}\right]\right\}dy \tag{A14}$$

A second integration gives

$$\overline{G}_{SS} = \frac{1}{b}\left\{\frac{b^2}{2}\left[\left(\frac{y^2}{2b}\right)-\left(\frac{y^3}{3b^2}\right)\right]\right\}_0^b + \frac{1}{ab}\left\{\frac{4}{b}\sum_{n=1}^{\infty}\frac{cos\left(\frac{\pi(2n-1)y}{b}\right)}{\left[\frac{\pi(2n-1)}{b}\right]^5}\left[\frac{\left[1-e^{-\frac{\pi(2n-1)a}{b}}\right]^2}{1-e^{-\frac{2\pi(2n-1)a}{b}}}\right]\right\}_0^b \tag{A15}$$

This expression evaluation leads to Eq. 8 in the text.

Boundary Flux ($\frac{dG(0,y;t_D)}{dx}$, $\int_0^b\frac{dG(0,y;t_D)}{dx}dy$, $\frac{dG(x,0;t)}{dy}$, *and* $\int_0^a\frac{dG(x,0;t)}{dy}dx$).

We have

$$\frac{dG(x,y;t_D)}{dx}=\frac{d}{dx}\left\{\begin{array}{c}\frac{b^2}{2}\left(\frac{y}{b}\right)\left[1-\left(\frac{y}{b}\right)\right]-\frac{4}{b}\sum_n\frac{sin\left(\frac{\pi(2n-1)y}{b}\right)}{\left[\frac{\pi(2n-1)}{b}\right]^3}\left[\frac{(E_1+E_2-E_3-E_4)}{\left(1-e^{-\frac{2\pi(2n-1)a}{b}}\right)}\right]\\ -\frac{16}{\pi^4}\sum_{l,m}exp\left[-\pi^2\left(\frac{(2l-1)^2}{a^2}+\frac{(2m-1)^2}{b^2}\right)t_D\right]\cdot\frac{sin\left(\frac{\pi(2l-1)x}{a}\right)sin\left(\frac{\pi(2m-1)y}{b}\right)}{(2l-1)(2m-1)\left(\frac{(2l-1)^2}{a^2}+\frac{(2m-1)^2}{b^2}\right)}\end{array}\right\} \tag{A16}$$

Leading to

$$\frac{dG(x,y;t_D)}{dx}=-\frac{4\pi}{b^2}\sum_n\frac{n\cdot sin\left(\frac{\pi(2n-1)y}{b}\right)}{\left[\frac{\pi(2n-1)}{b}\right]^3}\left[\frac{(-E_1+E_2+E_3-E_4)}{\left(1-e^{-\frac{2\pi(2n-1)a}{b}}\right)}\right] \tag{A17}$$

$$-\frac{16}{\pi^3 a}\sum_{l,m}exp\left[-\pi^2\left(\frac{(2l-1)^2}{a^2}+\frac{(2m-1)^2}{b^2}\right)t_D\right]\cdot\frac{cos\left(\frac{\pi(2l-1)x}{a}\right)sin\left(\frac{\pi(2m-1)y}{b}\right)}{(2m-1)\left(\frac{(2l-1)^2}{a^2}+\frac{(2m-1)^2}{b^2}\right)}$$

Evaluating this expression at the boundary, x = 0, gives the boundary flux distribution.

$$\frac{dG(0,y;t_D)}{dx}=\frac{4b}{\pi^2}\sum_n\frac{n\cdot sin\left(\frac{\pi(2n-1)y}{b}\right)}{(2n-1)^3}\left[\frac{\left(1-e^{-\frac{\pi(2n-1)a}{b}}\right)^2}{\left(1-e^{-\frac{2\pi(2n-1)a}{b}}\right)}\right]-\frac{16a}{\pi^3}\sum_{l,m}\frac{exp\left[-\frac{\pi^2}{a^2}\left((2l-1)^2+\left(\frac{a}{b}\right)^2(2m-1)^2\right)t_D\right]\cdot sin\left(\frac{\pi(2m-1)y}{b}\right)}{(2m-1)(2l-1)^2+\left(\frac{a}{b}\right)^2(2m-1)^3} \tag{A18}$$

For total flux, one must integrate across the boundary.

$$\int_0^b\frac{dG(0,y;t_D)}{dx}dy=-\frac{4\pi}{b^2}\int_0^b\sum_n\frac{n\cdot sin\left(\frac{\pi(2n-1)y}{b}\right)}{\left[\frac{\pi(2n-1)}{b}\right]^3}\left[\frac{\left(-1+e^{-\frac{\pi(2n-1)a}{b}}+e^{-\frac{\pi(2n-1)a}{b}}-e^{-\frac{2\pi(2n-1)a}{b}}\right)}{\left(1-e^{-\frac{2\pi(2n-1)a}{b}}\right)}\right]dy\ \frac{16a}{\pi^3}\int_0^b\sum_{l,m}\frac{exp\left[-\frac{\pi^2}{a^2}\left((2l-1)^2+\left(\frac{a}{b}\right)^2(2m-1)^2\right)t_D\right]\cdot sin\left(\frac{\pi(2m-1)y}{b}\right)}{(2m-1)(2l-1)^2+\left(\frac{a}{b}\right)^2(2m-1)^3}dy \tag{A19}$$

This reduces to a per unit area total flux

$$\int_0^b \frac{dG(0,y;t_D)}{dx}dy = \frac{8}{\pi^3}\left(\frac{b}{a}\right)\sum_n \frac{n}{(2n-1)^4}\left[\frac{\left(1-e^{-\frac{\pi(2n-1)a}{b}}\right)^2}{\left(1-e^{-\frac{2\pi(2n-1)a}{b}}\right)}\right] - \frac{32}{\pi^4}\sum_{l,m}\frac{exp\left[-\frac{\pi^2}{a^2}\left((2l-1)^2+\left(\frac{a}{b}\right)^2(2m-1)^2\right)t_D\right]}{(2m-1)^2(2l-1)^2+\left(\frac{a}{b}\right)^2(2m-1)^4} \quad \text{(A20)}$$

Similarly, we obtain Eqs. 13 and 15 in the text for the alternate boundary flux.

Acknowledgments This work was funded by Nazarbayev University Faculty Development Competitive Research Grant 17155628.

Availability of data and material Available upon specific request.

Code availability Unsupported.

Authors' contributions Hazlett primary development, computation, and manuscript development.

Younis consultation and editorial contribution.

MSC 52–08, 76S05, 31A10, 65 M80.

Declarations

Conflicts of interest/competing interests None.

References

1. Chen, Z.X.: Transient flow of slightly compressible fluids through double-porosity, double-permeability systems-a state-of-the-art review. Transp. Porous Media. **4**(2), 147–184 (1989)
2. Pruess, K., Narasimhan, T.N.: A practical method for modeling fluid and heat flow in fractured porous media. Soc. Pet. Eng. J. **25**(1), 14–26 (1985)
3. Bosma, S.B.M., Hajibeygi, H., Tene, M., Tchelepi, H.A.: Multiscale finite volume method for discrete fracture modeling with unstructured grids (MS-DFM). J. Comput. Phys. **351**, 145–164 (2017). https://doi.org/10.1016/j.jcp.2017.09.032
4. Xu, Y., Sepehrnoori, K.: Development of an embedded discrete fracture model for field-scale reservoir simulation with complex corner-point grids. Soc. Pet. Eng., August 1. **24**, 1552–1575 (2019). https://doi.org/10.2118/195572-PA
5. Barenblatt, G.I., Zheltov, I.P., Kochina, I.N.: Basic concepts in the theory of seepage of homogeneous liquids in fissured rocks. J. Appl. Math. Mech. **24**, 1286–1303 (1960). https://doi.org/10.1016/0021-8928(60)90107-6
6. Lshimoto, K.: Improved Matrix, Fracture fluid transfer function in dual porosity models. SPE 17599, presented at the SPE International Meeting on Petroleum Engineering, Tianjin, China, November 1–4 (1988)
7. Chang, M.: Deriving the Shape Factor of a Fractured Rock Matrix. Technical Report NIPER-696 (DE93000170). Bartlesville, Oklahoma: NIPER (1993)
8. Sarma, P.: New Transfer Functions for Simulation of Naturally Fractured Reservoirs with Dual Porosity Models, MS Thesis, Stanford University (2003)
9. Tellapaneni, P.K., Putra, E., Schechter, D.S.: Usage of x-ray CT for empirical transfer functions in dual porosity simulation. Paper 2004–246 presented at the Petroleum Society's 5th Canadian International Petroleum Conference, Calgary, June 8–10 (2004)
10. Sarma, P., Aziz, K.: New transfer functions for simulation of naturally fractured reservoirs with dual porosity models. SPEJ (September). **11**(03), 328–340 (2006)
11. Maier, C., Geiger, S.: Combining unstructured grids, discrete fracture representation and dual-porosity models for improved simulation of naturally fractured reservoirs. Soc. Pet. Eng., September 16. (2013). https://doi.org/10.2118/166049-MS
12. Belani, A.K., Jalali, Y.: Estimation of matrix block size distribution in naturally fractured reservoirs. Soc. Pet. Eng.. January 1. (1988). https://doi.org/10.2118/18171-MS
13. Gong, J., Rossen, W.R.: Shape factor for dual-permeability fractured reservoir simulation: effect of non-uniform flow in 2D fracture network. Fuel. **184**, 81–88 (2016)
14. Amiry, M.T.: Modeling Flow Behavior in Naturally Fractured Reservoirs. PhD Dissertation, University of Leoben, Austria. (2014)
15. Hazlett, R.D., Babu, D.K.: Discrete wellbore and fracture productivity modeling for unconventional wells and unconventional reservoirs. SPEJ. **19**(01), 19–33 (2014)
16. Hazlett, R.D., Babu, D.K.: Transient inflow performance modeling from analytic line source solutions for arbitrary trajectory wells. SPEJ. **23**(3), 906–918 (2018). https://doi.org/10.2118/189463-PA
17. Hazlett, R.: Flux Characterization in heterogeneous transport problems by the boundary integral method. In: Constanda, C., et al. (eds.) Integral Methods in Science and Engineering, vol. 2, Chapter 12. Springer International Publishing (2017). https://doi.org/10.1007/978-3-319-59387-6_12

18. Carslaw, H.S., Jaegar, J.C.: Conduction of Heat in Solids. Oxford University Press, Oxford (1959)
19. Newman, A.B.: Heating and cooling rectangular and cylindrical solids. Ind. Eng. Chem. **28**(5), 545–548 (1936)
20. McCann, R.C., Hazlett, R.D., Babu, D.K.: (2001, April) Highly accurate approximations of Green's and Neumann functions on rectangular domains. Proc. R. Soc. London A: Math. Phys. Eng. Sci. **457**, 767–772 (2008)
21. Bao, A., Hazlett, R.D., Babu, D.K.: A discrete, arbitrarily oriented 3D plane-source analytical solution to the diffusivity equation for modeling reservoir fluid flow. *SPEJ* (May 1) 1–15. **22**, 1609–1623 (2017). https://doi.org/10.2118/185180-PA
22. Gradshtein, I.S., Ryzhik, I.M.: Table of Integrals, Series, and Products. Academic Press, Amsterdam (1980)